

SCAN-BEST: Sub-6GHz-Aided Near-field Beam Selection with Formal Reliability Guarantees

Weicao Deng, *Graduate Student Member, IEEE*, Binpu Shi, *Graduate Student Member, IEEE*,
Min Li, *Member, IEEE*, and Osvaldo Simeone, *Fellow, IEEE*

Abstract—As millimeter-wave (mmWave) MIMO systems adopt larger antenna arrays, near-field propagation becomes increasingly prominent, especially for users close to the transmitter. Traditional far-field beam training methods become inadequate, while near-field training faces the challenge of large codebooks due to the need to resolve both angular and distance domains. To reduce in-band training overhead, prior work has proposed to leverage the spatial-temporal congruence between sub-6 GHz (sub-6G) and mmWave channels to predict the best mmWave beam within a near-field codebook from sub-6G channel estimates. To cope with the uncertainty caused by sub-6G/mmWave differences, we introduce a novel Sub-6G Channel Aided Near-field BEam SelecTion (SCAN-BEST) framework that wraps around any beam predictor to produce candidate beam subset with formal suboptimality guarantees. The proposed SCAN-BEST builds on conformal risk control (CRC), and is calibrated offline using limited calibration data. Its performance guarantees apply even in the presence of statistical shifts between calibration and deployment. Numerical results validate the theoretical properties and efficiency of SCAN-BEST.

Index Terms—Near-field, beam selection, conformal risk control, sub-6G channel, deep learning.

I. INTRODUCTION

Millimeter-wave (mmWave) and extremely large-scale massive multiple-input multiple-output (XL-MIMO) are recognized as key enablers for 6G communication systems [1], [2]. However, their adoption introduces unique challenges due to the high operating frequencies and to the large antenna array sizes, which result in a substantial increase in the Rayleigh distance—from a few meters to several hundred meters [3]. This significantly expands the near-field region, where electromagnetic waves must be accurately modeled using spherical wavefronts rather than planar approximations [4]. Communication quality in this regime becomes highly susceptible to blockages [5], presenting significant challenges for channel state information (CSI) acquisition and beamforming design.

The work of Osvaldo Simeone was partially supported by the European Union's Horizon Europe project CENTRIC (101096379), by the Open Fellowships of the EPSRC (EP/W024101/1) and by the EPSRC project (EP/X011852/1).

Weicao Deng, Binpu Shi, and Min Li are with the College of Information Science and Electronic Engineering and Zhejiang Provincial Key Laboratory of Multi-Modal Communication Networks and Intelligent Information Processing, Zhejiang University, Hangzhou 310027, China (e-mail: {caowd, bp.shi, min.li}@zju.edu.cn). (*Corresponding authors: Min Li.*)

Osvaldo Simeone is with the King's Communications, Learning & Information Processing (KCLIP) lab within the Centre for Intelligent Information Processing Systems (CIIPS), Department of Engineering, King's College London, London WC2R 2LS, U.K. (e-mail: osvaldo.simeone@kcl.ac.uk).

This work explores the idea of using sub-6 GHz (sub-6G) channel data to enhance mmWave communication. As illustrated in Fig. 1, sub-6G and mmWave channels exhibit similar power delay profiles (PDPs) [6], [7]. This congruence suggests the potential to extract both angular and distance information from sub-6G channels to facilitate near-field beam selection. Nonetheless, significant challenges remain due to the inherent differences between sub-6G and mmWave channels, such as variations in path parameters and discrepancies in angular and temporal resolutions. These differences introduce uncertainties when mapping sub-6G channel data to mmWave beams, as illustrated by the dominant path differences in Fig. 1b. Additionally, ensuring guaranteed performance for near-field beam selection remains an open research question and a critical challenge.

A. Related Works and Motivations

To address these challenges, a significant number of works [8]–[12] have focused on the angle and distance characteristics of near-field channels, proposing various beam training approaches. For instance, reference [8] introduced on-grid/off-grid polar-domain simultaneous orthogonal matching pursuit (OMP) channel estimation methods that exploit the polar-domain sparsity of near-field channels. Reference [9] developed a two-phase beam training scheme that divides the two-dimensional search in the polar-domain codebook into two sequential angular and distance domain searches. Similarly, reference [10] proposed a two-stage hierarchical beam training method. In the first stage, the central sub-array is used to perform a coarse search for the user direction in the angular domain. In the second stage, a fine-grained search for the user's direction and distance is conducted in the polar domain.

Inspired by the integration of wireless communication and artificial intelligence (AI) [13], reference [11] proposed frameworks to predict the optimal angle and distance using extensive near-field beam training. Likewise, reference [12] developed a framework that leverages received signals from the far-field wide beam training. These studies rely solely on in-band measurements and often struggle to achieve optimal performance under a limited pilot budget or low signal-to-noise ratio (SNR) conditions.

Several studies [15]–[18] have utilized the angular domain congruence between sub-6G and mmWave channels to assist the far-field beam selection or beamforming. Building on [15], reference [19] proposed a complex simultaneous logit-weighted block OMP algorithm for near-field channel

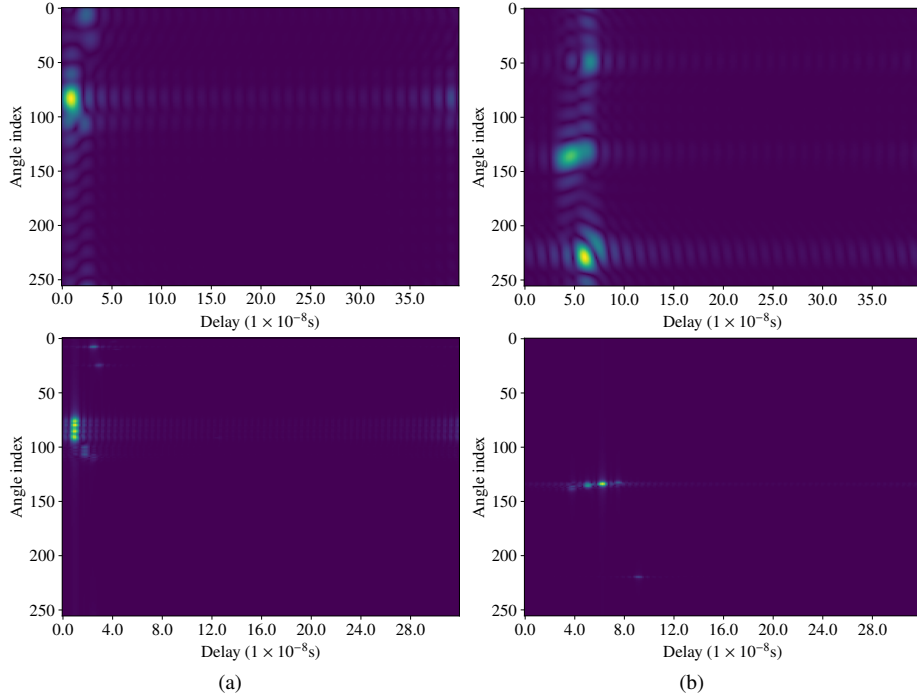


Fig. 1. An illustration of spatial and temporal correlation between sub-6G and mmWave channels. Each column represents a pair of sub-6G (upper row) and mmWave (lower row) augmented angle and delay profiles. The first column describes a line-of-sight (LoS) condition, while the second column represents a non-LoS (NLoS) condition [14].

estimation, which leverages the angular domain congruence between sub-6G and mmWave channel to design the training codebook and assign weights. However, in the context of near-field beamforming or channel estimation, it's not just the angle information that is requisite; distance information is similarly necessary. Moreover, the inherent channel variances between sub-6G and mmWave frequencies present a significant challenge to reliably mapping sub-6G information to mmWave beam with performance guarantee.

Conformal risk control (CRC) is a recent technique that aims at providing risk guarantees for the set-based decision, which has been extensively studied in numerous previous works in mathematics and statistics [20], [21], been applied to a number of engineering settings including computer vision, natural language processing, information retrieval systems [22], health imaging [23], anomaly detection [24], and telecommunication [25], [26]. Extensions of CRC include cross-validation-based method [27] and online strategies [28], [29].

In the context of wireless communication, reference [30] was the first to explore the application of conformal prediction (CP), a precursor of CRC [21], to the design of AI for communication systems, with focus on demodulation, modulation classification, and channel prediction. Additionally, reference [31] investigated federated CP in a wireless setting, proposing a novel wireless federated CP framework for federated reliable inference, and the work [32] extended the approach to a fully decentralized setting. Inspired by the prior works, this work further explores the use of CRC to enable reliable near-field beam selection.

B. Main Contributions

The correlation between sub-6G and mmWave channels illustrated in Fig. 1 offers promising potential for enabling low-overhead near-field beam selection, surpassing traditional in-band schemes. However, the non-negligible discrepancies between these two frequency bands introduce substantial uncertainty in predicting mmWave near-field beams based on sub-6G information. To address this challenge, we develop Sub-6GHz Channel Aided Near-field BEam Selection (SCAN-BEST), a framework combining deep learning for beam prediction with CRC to ensure reliability guarantee. Our main contributions are summarized as follows:

- 1) We develop the SCAN-BEST, a framework that wraps around any sub-6G channel-aided near-field beam prediction. Through a CRC-based scheme, SCAN-BEST efficiently constructs a near-field candidate beam subset that formally meets a target suboptimality ratio with respect to the best beam in this set with a prescribed probability. A weighted variant of SCAN-BEST is developed based on weighted CRC [33] to extend the performance guarantees of SCAN-BEST to satisfy a statistical shift between calibration and test data.
- 2) We conduct comprehensive numerical simulations to validate the efficiency of SCAN-BEST by comparing it with various sub-6G-based and mmWave baselines. The performance is evaluated across different target suboptimal rates and calibration dataset sizes. We also examine the scalability of SCAN-BEST by varying the quality of sub-6G data, including changes in the number of sub-6G antennas and the power levels in sub-6G channel estimation.

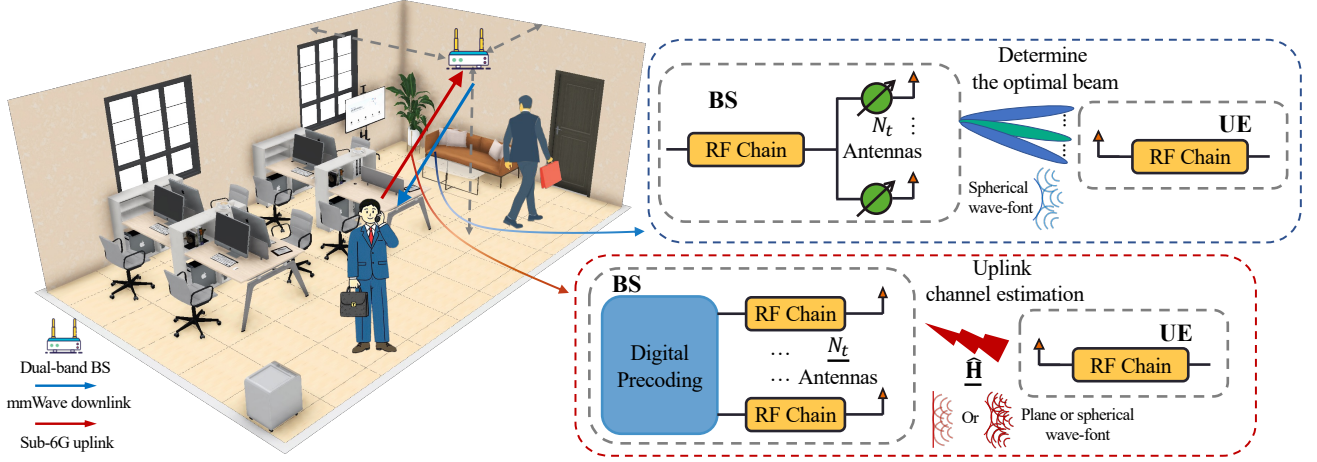


Fig. 2. An illustration of system model and beamforming architecture.

tion. Moreover, we validate the performance of SCAN-BEST in the presence of the covariate shift between the calibration and test data via weighted CRC.

The remainder of this paper is organized as follows. Section II describes the system model and formulates the problem of sub-6G channel-aided near-field beam selection as well as its calibration. Section III elaborates on the proposed SCAN-BEST framework from its implementation. In Section IV-A, we present and discuss the numerical results to validate the effectiveness of SCAN-BEST. Section V provides conclusions for this paper.

Notations: Scalars, vectors and matrices are respectively denoted by lower/upper case, boldface lower case and boldface upper case letters. Notation \mathbf{I}_m represents an $m \times m$ identity matrix. $\mathcal{CN}(0, \sigma^2)$ is a zero-mean complex Gaussian distribution with variance σ^2 . The function $\text{card}(\mathcal{X})$ returns the cardinality of set \mathcal{X} . The notation $A \times B$ is also used for the Cartesian product of the sets $\{1, 2, \dots, A\}$ and $\{1, 2, \dots, B\}$ with integers A and B . Moreover, to distinguish between the sub-6G system and mmWave system, we use (\cdot) to indicate parameters corresponding to the sub-6G system, as exemplified by \underline{x} .

II. SYSTEM MODEL AND PROBLEM FORMULATION

As depicted in Fig. 2, as in [15]–[17], we consider a dual-band system comprising a BS and single UE. Both the BS and UE are equipped with two transceivers that operate in sub-6G frequencies and mmWave frequencies, respectively. The UE is assumed to have a single antenna in both mmWave and sub-6G frequencies. As for the BS, the mmWave system is equipped a uniform linear array (ULA) comprising N_t antennas with half-wavelength spacing, and it adopts a fully analog beamforming architecture. In contrast, its sub-6G system is equipped with a ULA of \underline{N}_t antennas with half-wavelength spacing, and it employs a fully digital beamforming architecture. In the rest of this section, we will define the mmWave and sub-6G radio interfaces, as well as the problem definition.

A. MmWave Downlink Communication and Channel Model

We consider a wideband mmWave orthogonal frequency division multiplex (OFDM) system operating at the center frequency f_c with a total system bandwidth W and K subcarriers. The sampling period T_s is given by $T_s = 1/W$, and the number of channel taps at the resolution T_s is denoted as D . The signal transmitted at the k -th subcarrier $s_{t,k} \in \mathbb{C}$ follows the complex Gaussian distribution $\mathcal{CN}(0, P_t/K)$ with P_t being the total transmitting power. Let \mathbf{f} be the analog beam applied by the BS. The received signal of the UE at the k -th subcarrier $y_k \in \mathbb{C}$ can be written as [34]

$$y_k = \mathbf{h}_k^H \mathbf{f} s_{t,k} + n_k, \quad (1)$$

where $\mathbf{h}_k^H \in \mathbb{C}^{1 \times N_t}$ denotes the frequency-domain channel from the BS to the UE at the k -th subcarrier, and $n_k \sim \mathcal{CN}(0, \sigma_n^2)$ is the additive noise with the variance σ_n^2 .

We adopt a wideband geometric channel model consisting of a total of L paths between the BS and the UE. To account for large arrays, we model the extended near-field range via spherical wave-fronts [3]. The channel gain, angle of departure (AoD), and time of arrival (ToA) of the l -th path between the BS and the UE are denoted by g_l , θ_l , and τ_l , respectively. Furthermore, if the l -th path is in line of sight (LOS), the additional path parameter r_l is used to denote the distance between the BS and the UE, while otherwise, r_l denotes the distance between the BS and the scatterer in the l -th path of the UE. Overall, the delay- d mmWave channel tap from the BS to UE, denoted as $\mathbf{h}_d^H \in \mathbb{C}^{1 \times N_t}$, is given by [15]

$$\mathbf{h}_d^H = \sqrt{N_t} \sum_{l=1}^L g_l p(dT_s - \tau_l) \mathbf{b}^H(\theta_l, r_l), \quad (2)$$

for $d = 1, \dots, D$, where $p(\cdot)$ denote the pulse-shaping filter, and the steering vector $\mathbf{b}^H(\theta_l, r_l)$ is given by

$$\mathbf{b}^H(\theta_l, r_l) = \frac{1}{N_t} [e^{-j2\pi(r_l^{(0)} - r_l)}, \dots, e^{-j2\pi(r_l^{(N_t-1)} - r_l)}], \quad (3)$$

with $r_l^{(n)} = \sqrt{r_l^2 + \delta^{(n)2}(\lambda/2)^2 - r_l\theta_l\delta^{(n)}\lambda}$, with $\delta^{(n)} = (2n - N_t - 1)/2$ [3]. Based on the delay- d channel tap in (2), the frequency-domain mmWave channel at the k -th subcarrier,

$\mathbf{h}_k^H \in \mathbb{C}^{1 \times N_t}$ is given by

$$\mathbf{h}_k^H = \sum_{d=1}^D \mathbf{h}_d^H e^{-j \frac{2\pi k}{K} d}, \quad (4)$$

for $k = 1, \dots, K$. For notational convenience, we denote the overall frequency-domain mmWave OFDM channel as $\mathbf{H} \triangleq [\mathbf{h}_1, \dots, \mathbf{h}_K]^H$.

B. Sub-6G Channel Model and Uplink Channel Estimation

The sub-6G link between BS and UE operates at the center frequency f_c , with a total bandwidth W , number of subcarriers K , sampling period $T_s = 1/W$, and number of channel taps D . Due to the more abundant scattering and diffraction of sub-6G propagation with respect to (w.r.t.) the mmWave band, there typically exist $\underline{L} > L$ paths between the BS and UE [6], [15]. We denote the gain, angle of arrival (AoA), time of arrival (ToA) of the l -th channel path with g_l , θ_l , and τ_l , respectively. Due to the shorter Rayleigh distance of the sub-6G system compared to the mmWave system, the UE is likely to be located in either the far-field or near-field region of the sub-6G system. Thus, similar to the latest work [19], the sub-6G channel between the BS and the UE is modeled under two cases.

When the UE is located in the far-field region, the delay- d sub-6G channel tap from the UE to BS $\mathbf{h}_d \in \mathbb{C}^{N_t \times 1}$ is given by [15]

$$\mathbf{h}_d = \sum_{l=1}^{\underline{L}} g_l p(dT_s - \tau_l) \mathbf{a}(\theta_l), \quad (5)$$

for $d = 1, \dots, \underline{D}$, where the steering vector $\mathbf{a}(\theta_l)$ is

$$\mathbf{a}(\theta_l) = [1, e^{-j\pi \sin(\theta_l)}, \dots, e^{-j\pi(N_t-1)\sin(\theta_l)}]^T. \quad (6)$$

When the UE is located in the near-field region, \mathbf{h}_d is similar to the mmWave near-field one and thus will not be elaborated further here.

Using (5), the frequency-domain sub-6G channel at the k -th subcarrier $\mathbf{h}_k \in \mathbb{C}^{N_t \times 1}$ is given by

$$\mathbf{h}_k = \sum_{d=1}^D \mathbf{h}_d e^{-j \frac{2\pi k}{K} d}, \quad (7)$$

for $k = 1, \dots, K$.

Through a fully digital receiver architecture in the sub-6G system, the frequency-domain channels at the K subcarriers is estimated via sub-6G pilot transmission. To this end, the UE sends the uplink pilot signal $s_{p,k} = \sqrt{P_s/K}$ at the k -th subcarrier with P_s being the total power of the pilot signal. The received signals by the BS at the k -th subcarrier $\mathbf{y}_{p,k}$ can be written as

$$\mathbf{y}_{p,k} = \mathbf{h}_k s_{p,k} + \mathbf{n}_k, \quad (8)$$

where $\mathbf{n}_k \sim \mathcal{CN}(0, \sigma_n^2 \mathbf{I}_{N_t})$ denotes the noise vector with σ_n^2 being the sub-6G noise power. The frequency-domain sub-6G channel estimate at the k -th subcarrier $\hat{\mathbf{h}}_k$ can be obtained via a low-complexity least square (LS) algorithm, which is given by

$$\hat{\mathbf{h}}_k = \mathbf{y}_{p,k} s_{p,k}^{-1}. \quad (9)$$

We denote the frequency-domain sub-6G OFDM channel estimate as $\hat{\mathbf{H}} \triangleq [\hat{\mathbf{h}}_1, \dots, \hat{\mathbf{h}}_K]^H$.

C. Problem Formulation

Following prior works [9], [35], we consider the problem of beam selection from a predefined near-field codebook. Specifically, we adopt the polar codebook introduced in [8], denoted as $\mathcal{W} \triangleq (\mathbf{w}_{n,s})_{N_t \times S}$, where the numbers of candidate angles and distances are equal to the number of mmWave transmit antennas, N_t , and to an integer parameter S , respectively. Each beam $\mathbf{w}_{n,s} = \mathbf{b}(\theta_n, r_{n,s})$ in the set \mathcal{W} corresponds to the (n, s) -th angle-distance sector, with

$$\begin{aligned} \theta_n &= \arcsin\left(\frac{-1 + 2n}{N_t}\right), \\ r_{n,s} &= \frac{(1 - \sin(\theta_n))^2 N_t^2 d^2}{2s\beta^2\lambda}, \end{aligned} \quad (10)$$

where β is the correlation parameter between neighboring beams [8].

For a given mmWave channel sample \mathbf{H} , the *optimal beam* \mathbf{f}^* is defined as the beam in set \mathcal{W} that maximizes the average spectral efficiency, i.e., as

$$\mathbf{f}^* = \mathbf{w}_{n^*, s^*} = \arg \max_{\mathbf{w}_{n,s} \in \mathcal{W}} R(\mathbf{w}_{n,s}, \mathbf{H}), \quad (11)$$

where the average spectral efficiency is over all subcarriers given by

$$R(\mathbf{w}_{n,s}, \mathbf{H}) = \frac{1}{K} \sum_{k=1}^K \log_2 \left(1 + \frac{P_t |\mathbf{h}_k^H \mathbf{w}_{n,s}|^2}{\sigma_n^2} \right). \quad (12)$$

Most previous works [8]–[12] have focused on in-band beam training to determine the optimal near-field beam (11). However, these methods typically require a substantial number of pilots. As in [16], [19], [36], [37], we explore the potential of sub-6G information for near-field beam selection to reduce pilot overhead. Specifically, in order to account for the inherent uncertainty associated with the mapping from sub-6G information to mmWave beam selection, we propose to operate as follows:

- 1) **Sub-6G-based candidate beam selection:** Construct a candidate beam subset $\mathcal{C}(\hat{\mathbf{H}})$ based on the sub-6G channel estimate $\hat{\mathbf{H}}$.
- 2) **MmWave beam training:** Perform limited mmWave beam training within the subset $\mathcal{C}(\hat{\mathbf{H}})$ to choose a beam $\mathbf{f} = \mathbf{w}_{\hat{n}, \hat{s}} \in \mathcal{C}(\hat{\mathbf{H}})$.

Traditional designs for candidate beam selection, such as top- K [16] and probability sum-based methods [37] lack theoretical guarantees on the quality of the pre-selected candidate beam subset. Thus, the subsequent mmWave beam training may fail to return a well-performing beam in the codebook \mathcal{W} with a probability exceeding user's requirements.

To formalize theoretical guarantees for the candidate beam subset, we first introduce a relaxed notion of beam optimality. To this end, for any beam \mathbf{f} , we denote the *suboptimality ratio* as the ratio of the rate achieved by beam \mathbf{f} and the rate of the optimal beam \mathbf{f}^* , i.e.,

$$r(\mathbf{f}, \mathbf{H}) = \frac{R(\mathbf{f}, \mathbf{H})}{R(\mathbf{f}^*, \mathbf{H})}. \quad (13)$$

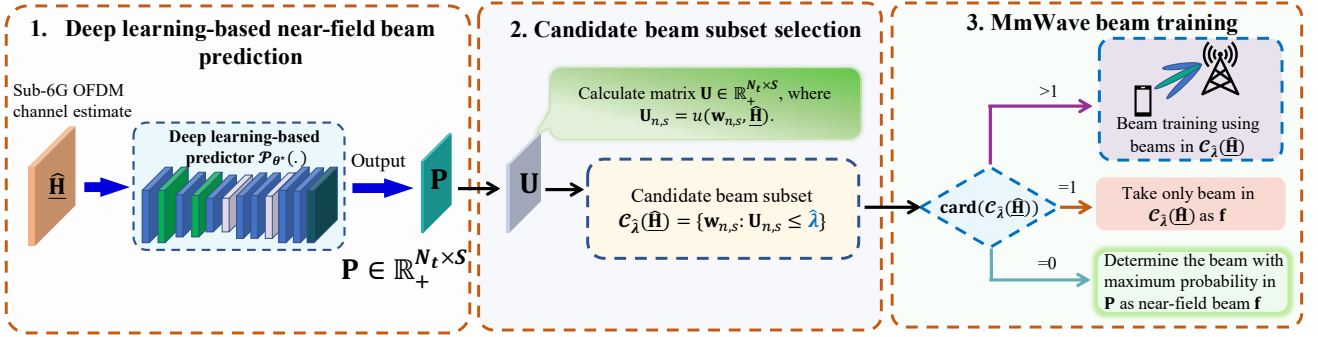


Fig. 3. The overall design of the SCAN-BEST framework.

Then, a beam \mathbf{f} is said to be ϵ -suboptimal if it satisfies the condition

$$r(\mathbf{f}, \mathbf{H}) \geq 1 - \epsilon, \quad (14)$$

where ϵ , with $0 \leq \epsilon \leq 1$, is the suboptimality factor. In practice, the parameter ϵ is typically set in the range $0 \leq \epsilon \leq 0.2$, with $\epsilon = 0$ identifying the optimal beam \mathbf{f}^* .

In this paper, unlike prior studies [8], [9], [35], we aim to design a sub-6G information-aided solution that guarantees a user-specified probability $1 - \alpha \in [0, 1]$ of identifying an ϵ -suboptimal beam. Specifically, given a target suboptimal ratio ϵ , we wish to ensure that the probability of failing to obtain an ϵ -suboptimal beam is no larger than α , i.e.,

$$\Pr(r(\mathbf{f}, \mathbf{H}) < 1 - \epsilon) \leq \alpha, \quad (15)$$

where the probability is taken over mmWave channels \mathbf{H} . Condition (15) is satisfied, for a well-designed mmWave training phase, as long as the probability that the candidate beam subset $\mathcal{C}(\hat{\mathbf{H}})$ contains none beams with suboptimality smaller than ϵ does not exceed α , i.e.,

$$\Pr(\nexists \mathbf{w} \in \mathcal{C}(\hat{\mathbf{H}}) : r(\mathbf{w}, \mathbf{H}) < 1 - \epsilon) \leq \alpha. \quad (16)$$

We will refer to the probability in (16) as the *miscoverage probability*, and denote $1 - \alpha$ as *target coverage rate*.

III. SUB-6G CHANNEL AIDED NEAR-FIELD BEAM SELECTION FRAMEWORK

In this section, we first present an overview of SCAN-BEST, and then elaborate on its implementation.

A. Overview of SCAN-BEST

SCAN-BEST wraps around a deep learning-based beam predictor and on the statistical methodology of CRC [21]. For given suboptimality parameter ϵ and probability α , SCAN-BEST, as illustrated in Fig. 3, proceeds along the following three stages:

- 1) **Deep learning-based near-field beam prediction:** Based on sub-6G channel estimate, employ any pre-trained neural model to assign each beam in the codebook \mathcal{W} an estimated probability of being the optimal near-field beam [17].
- 2) **Sub-6G-based candidate beam subset selection:** Using the predicted probabilities for all candidate beams in \mathcal{W} , CRC is leveraged to select a near-field candidate beam

subset $\mathcal{C}(\hat{\mathbf{H}})$ that ensures the desired target coverage rate condition in (16).

- 3) **MmWave beam training:** The near-field beam is determined by performing limited beam training only along the beam within the candidate beam subset $\mathcal{C}(\hat{\mathbf{H}})$.

B. Deep Learning-based Near-Field Beam Prediction

In the first stage, a deep learning model is used to predict the probability of each beam in the codebook \mathcal{W} being the optimal near-field beam based sub-6G channel estimate $\hat{\mathbf{H}}$. To elaborate, introduce a probability matrix $\mathbf{P} \in [0, 1]^{N_t \times S}$, where the entry $\mathbf{P}_{n,s}$ represents the predicted probability that the beam $\mathbf{w}_{n,s}$ is the optimal near-field beam. The mapping between the sub-6G channel estimate $\hat{\mathbf{H}}$ and matrix \mathbf{P} , denoted as $\mathbf{P} = \mathcal{P}_\theta(\hat{\mathbf{H}})$, is parameterized with a vector θ .

In order to train the neural network mapping $\mathbf{P} = \mathcal{P}_\theta(\hat{\mathbf{H}})$, as in [17], one assumes the availability of a dataset $\mathcal{D}_{\text{tr}} \triangleq \{\hat{\mathbf{H}}_i, n_i^*, s_i^*\}_{i=1}^{N_{\text{tr}}}$ associating a sub-6G channel estimate $\hat{\mathbf{H}}_i$ with the corresponding index (n_i^*, s_i^*) of the optimal beam in (11). Training is typically done by minimizing the standard cross-entropy loss, yielding the optimized parameter [17]

$$\theta^* = \arg \max_{\theta} \left\{ - \sum_{i=1}^{N_{\text{tr}}} \log \mathcal{P}_{\theta, n_i^*, s_i^*}(\hat{\mathbf{H}}) \right\}, \quad (17)$$

where $\mathcal{P}_{\theta, n_i^*, s_i^*}(\hat{\mathbf{H}})$ is the (n_i^*, s_i^*) -th entry of matrix $\mathcal{P}_\theta(\hat{\mathbf{H}})$.

C. Sub-6G-based candidate beam subset Selection

Given the trained model $\mathcal{P}_{\theta^*}(\cdot)$ in (17), and given an input $\hat{\mathbf{H}}$, SCAN-BEST evaluates a negatively oriented score for beam $\mathbf{w}_{n,s}$, namely

$$u(n, s, \hat{\mathbf{H}}) = -\log P_{\max}(\hat{\mathbf{H}}) - \log \mathbf{P}_{n,s}(\hat{\mathbf{H}}), \quad (18)$$

where

$$\begin{aligned} \mathbf{P}_{n,s}(\hat{\mathbf{H}}) &= \mathcal{P}_{\theta^*, n, s}(\hat{\mathbf{H}}), \\ P_{\max}(\hat{\mathbf{H}}) &= \max_{n, s \in N_t \times S} \mathbf{P}_{n,s}(\hat{\mathbf{H}}). \end{aligned} \quad (19)$$

The term $-\log P_{\max}(\hat{\mathbf{H}})$ is referred to as the Rényi min-entropy for the predictive conditional probability $\mathcal{P}_{\theta^*}(\hat{\mathbf{H}})$, which provides a measure of the uncertainty of the model $\mathcal{P}_{\theta^*}(\cdot)$ regarding this prediction with input $\hat{\mathbf{H}}$ [38]. Adding this term to the negative log-likelihood $-\log \mathbf{P}_{n,s}(\hat{\mathbf{H}})$ degrades the score $u(n, s, \hat{\mathbf{H}})$ when the predictive uncertainty

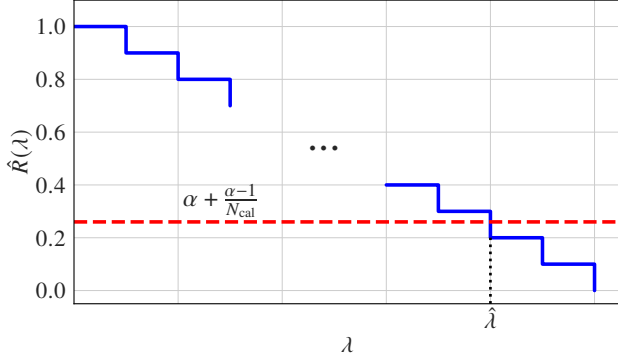


Fig. 4. A simple illustration of $\hat{R}(\lambda)$ (blue line), the orange line denotes the desired risk level.

is high. Recall, in fact, that a smaller value of the score $u(n, s, \hat{\mathbf{H}})$ indicates that the beam $\mathbf{w}_{n,s}$ is predicted to be more likely to be optimal.

The subset $\mathcal{C}_\lambda(\hat{\mathbf{H}})$ of candidate beams includes all beams in set \mathcal{W} whose scores (18) are no larger than a threshold λ , i.e.,

$$\mathcal{C}_\lambda(\hat{\mathbf{H}}) = \left\{ \mathbf{w}_{n,s} \in \mathcal{W} : u(n, s, \hat{\mathbf{H}}) \leq \lambda \right\}. \quad (20)$$

In order to select the threshold λ so that the coverage condition (16) is satisfied, we adopt CRC [21]. To this end, we assume a held-out calibration dataset $\mathcal{D}_{\text{cal}} \triangleq \{\hat{\mathbf{H}}_i, \mathbf{H}_i\}_{i=1}^{N_{\text{cal}}}$, where $\hat{\mathbf{H}}_i$ is the sub-6G channel estimate and \mathbf{H}_i is a corresponding ground-truth mmWave channel. Using the calibration dataset, the probability (16) is estimated, and the estimate is evaluated as a function of the threshold λ . This evaluation is leveraged to find a threshold λ that satisfies the inequality (16).

Specifically, the set $\mathcal{C}_\lambda(\hat{\mathbf{H}}_i)$ is evaluated using (20) for all calibration data points $i = 1, \dots, N_{\text{cal}}$. Then, the misscoverage probability (16) is estimated using the calibration data set as

$$\hat{R}(\lambda) = \frac{1}{N_{\text{cal}}} \sum_{i=1}^{N_{\text{cal}}} \mathbb{1} \left(\nexists \mathbf{w} \in \mathcal{C}_\lambda(\hat{\mathbf{H}}_i) : r(\mathbf{w}, \mathbf{H}_i) \geq 1 - \epsilon \right). \quad (21)$$

Proposition 1. The subset $\mathcal{C}_{\hat{\lambda}}(\hat{\mathbf{H}})$ in (20) with the threshold

$$\hat{\lambda} = \inf \left\{ \lambda \in \mathbb{R} : \hat{R}(\lambda) \leq \alpha + \frac{\alpha - 1}{N_{\text{cal}}} \right\} \quad (22)$$

attains the target coverage rate $1 - \alpha$ in (16) for any input $\hat{\mathbf{H}}$ and “any” predictive model $\mathcal{P}_{\theta^*}(\cdot)$.

Proof: The proof is deferred to Appendix A.

Accordingly, as illustrated in Fig. 4, the threshold is selected so that the misscoverage probability (21) satisfies the condition (16) with the caveat that the reliability requirement is made stricter—from α to $\alpha + (\alpha - 1)/N_{\text{cal}}$. Note that the added term in the coverage probability α decreases to zero as $N_{\text{cal}} \rightarrow \infty$.

Finding the threshold (22) is computationally straightforward given that the empirical risk $\hat{R}(\lambda)$ is monotonically non-increasing relative to λ (see Fig. 4). Furthermore, a threshold satisfying the condition (22) always exists, since the choice $\lambda = \max_{i \in \{1, \dots, N_{\text{cal}}\}} u(n_i^*, s_i^*, \hat{\mathbf{H}}_i)$ yields $\hat{R}(\lambda) = 0$. Following the properties of CRC [21], this choice of the threshold ensures the condition (16).

D. Addressing Covariate Shifts between Calibration and Test Data

The theoretical guarantees of CRC rely on the assumption that calibration and test data follow the same distribution. In this subsection, we consider a more general case, in which a covariate shift exists between the calibration and test data. In this case, the distribution of sub-6G channel estimates $\hat{\mathbf{H}}$ in the calibration dataset, denoted as $\Gamma_c(\hat{\mathbf{H}})$, differs from that in the test dataset, denoted by $\Gamma_t(\hat{\mathbf{H}})$. To address this distribution mismatch, we adopt the weighted CRC method [33].

Weighted CRC assigns importance weights to each sample in the calibration dataset so as to compensate for the discrepancy between calibration and test data. Specifically, the importance weight for the i -th calibration sample and the importance weight for the test input $\hat{\mathbf{H}}'$, are defined as

$$\omega_i = \frac{p_i}{\sum_{j=1}^{N_{\text{cal}}} p_j + p'}, \text{ and } \omega' = \frac{p'}{\sum_{j=1}^{N_{\text{cal}}} p_j + p'}, \quad (23)$$

respectively, where the likelihood ratio p_i for $i = 1, \dots, N_{\text{cal}}$ and p' are given by

$$p_i = \frac{\Gamma_t(\hat{\mathbf{H}}_i)}{\Gamma_c(\hat{\mathbf{H}}_i)}, \text{ and } p' = \frac{\Gamma_t(\hat{\mathbf{H}}')}{\Gamma_c(\hat{\mathbf{H}}')}. \quad (24)$$

With the weights (23), the weighted misscoverage probability (21) is defined as

$$\tilde{R}(\lambda) = \sum_{i=1}^{N_{\text{cal}}} \omega_i \mathbb{1} \left(\nexists \mathbf{w} \in \mathcal{C}_\lambda(\hat{\mathbf{H}}_i) : r(\mathbf{w}, \mathbf{H}_i) \geq 1 - \epsilon \right). \quad (25)$$

Intuitively, this estimate assigns more importance to the samples in the calibration dataset that are more likely to be samples from the test distribution.

Proposition 2. The subset $\mathcal{C}_{\hat{\lambda}}(\hat{\mathbf{H}})$ in (20) with the threshold

$$\hat{\lambda} = \inf \left\{ \lambda \in \mathbb{R} : \tilde{R}(\lambda) \leq \alpha - \omega' \right\} \quad (26)$$

attains the target coverage rate $1 - \alpha$ in the test data.

Proof: The proof is deferred to Appendix B.

In practical implementations, the true densities $\Gamma_c(\cdot)$ and $\Gamma_t(\cdot)$ are unknown. Therefore, following [33], we estimate the importance weights using a pre-trained probabilistic classifier $g(\cdot)$ optimized to distinguish between samples from calibration and test distribution. Accordingly, the model $g(\cdot)$ outputs the probability that the test input $\hat{\mathbf{H}}'$ belongs to the test distribution. The estimated likelihood ratios \hat{p}_i for $i = 1, \dots, N_{\text{cal}}$ and \hat{p}' are then computed as

$$\hat{p}_i = \frac{g(\hat{\mathbf{H}}_i)}{1 - g(\hat{\mathbf{H}}_i)}, \text{ and } \hat{p}' = \frac{g(\hat{\mathbf{H}}')}{1 - g(\hat{\mathbf{H}}')}. \quad (27)$$

E. MmWave Beam Training

For a given input $\hat{\mathbf{H}}$, the candidate beam subset $\mathcal{C}_{\hat{\lambda}}(\hat{\mathbf{H}})$ may have any cardinality between zero and $N_t S$. Accordingly, the mmWave training stage operates as follows:

- 1) If the set $\mathcal{C}_{\hat{\lambda}}(\hat{\mathbf{H}})$ is empty, SCAN-BEST selects the most-likely beam corresponding to the maximum probability in \mathbf{P} as the final beam \mathbf{f} .
- 2) If the set $\mathcal{C}_{\hat{\lambda}}(\hat{\mathbf{H}})$ has cardinality equal to one, the only beam in $\mathcal{C}_{\hat{\lambda}}(\hat{\mathbf{H}})$ is selected as the final beam \mathbf{f} .

3) If the set $\mathcal{C}_{\hat{\lambda}}(\hat{\mathbf{H}})$ has cardinality larger than one, mmWave beam training is performed to select final beam \mathbf{f} .

MmWave training leverages the transmission of pilot symbols in the uplink of the mmWave band. To elaborate, let $s_{p,k} = \sqrt{P_s/K}$ denote the uplink pilot signal at the k -th subcarrier, where P_s represents the total power allocated for pilot transmission. When employing the beam $\mathbf{w} \in \mathcal{C}_{\hat{\lambda}}(\hat{\mathbf{H}})$, the corresponding received signal at the k -th subcarrier, denoted as $y_{\mathbf{w},k}$, is given by:

$$y_{\mathbf{w},k} = \mathbf{w}^T \mathbf{h}_k s_{p,k} + \mathbf{w}^T \mathbf{n}_k, \quad (28)$$

where $\mathbf{n}_k \sim \mathcal{CN}(\mathbf{0}, \sigma_n^2 \mathbf{I}_{N_t})$ denotes the noise vector with variance σ_n^2 . Based on the received signal (28), the final beam \mathbf{f} is selected as the beam corresponding to the maximum received power:

$$\mathbf{f} = \arg \max_{\mathbf{w} \in \mathcal{C}_{\hat{\lambda}}(\hat{\mathbf{H}})} \sum_{k=1}^K |y_{\mathbf{w},k}|^2. \quad (29)$$

If multiple pilots are transmitted per beam, the average power is computed in (29).

The entire implementation of SCAN-BEST framework is summarized in Algorithm 1.

Algorithm 1 SCAN-BEST

Input: Sub-6G OFDM channel estimates $\hat{\mathbf{H}}$, target miscoverage rate α

Output: Near-field beam \mathbf{f}

- 1: Produce the near-field beam probability matrix $\mathcal{P}_{\theta^*}(\hat{\mathbf{H}})$
 - 2: Construct near-field candidate beam subset $\mathcal{C}_{\hat{\lambda}}(\hat{\mathbf{H}})$ via (20)
 - 3: **if** $\mathcal{C}_{\hat{\lambda}}(\hat{\mathbf{H}})$ is empty, i.e., $\text{card}(\mathcal{C}_{\hat{\lambda}}(\hat{\mathbf{H}})) = 0$ **then**
 - 4: Identify the beam with the largest probability in $\mathbf{P} = \mathcal{P}_{\theta^*}$ as the near-field beam \mathbf{f}
 - 5: **else if** $\text{card}(\mathcal{C}_{\hat{\lambda}}(\hat{\mathbf{H}})) = 1$ **then**
 - 6: Assign the only beam in $\mathcal{C}_{\hat{\lambda}}(\hat{\mathbf{H}})$ as \mathbf{f}
 - 7: **else**
 - 8: Conduct uplink beam training using the beams in $\mathcal{C}_{\hat{\lambda}}(\hat{\mathbf{H}})$ and then select the beam with the strongest received signal power as \mathbf{f} using (29)
 - 9: **end if**
-

IV. NUMERICAL RESULTS

In this section, we present experimental results to validate the performance of SCAN-BEST.

A. Simulation Scenario and System Parameter Setup

As depicted in Fig. 5, we consider an indoor scenario within an area of dimensions 13.2 m \times 26.5 m. The BS with height 2.5 m, is located at the center of the area. The UE is randomly placed within the area, with a height of 1 m. The UE is assumed to be the height of 1 m, and it can be located anywhere within the room, leading to the LoS condition or NLoS conditions. More detailed system parameters are listed in Table I, with exceptions marked explicitly in the text.

We first collect a total of 10,000 samples from the above indoor scenario via a ray-tracing software [14], each of which consists of a pair of sub-6G channel estimate and true mmWave channel $\{\hat{\mathbf{H}}, \mathbf{H}\}$. These samples are randomly split for training, validating, calibration, and test, respectively, with the ratio of 50%, 10%, 20%, and 20%, respectively.

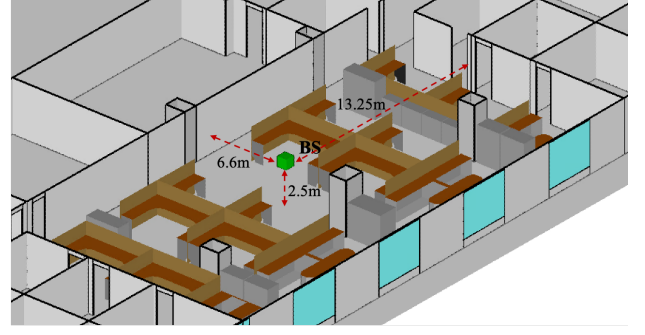


Fig. 5. An illustration of simulation setup.

TABLE I
SYSTEM PARAMETERS

Notations	Parameters	Values
$f_c, \underline{f_c}$	Operating frequency of mmWave, sub-6G system (GHz)	73, 3.5
W, \underline{W}	Bandwidth of mmWave, sub-6G system (MHz)	200, 80
K, \underline{K}	Number of subcarriers of mmWave, sub-6G system	64, 32
$N_t, \underline{N_t}$	Number of mmWave, sub-6G antennas at the BS	256, 16
P_t, P_s	Total power of mmWave downlink, uplink pilot (dBm)	25, 25
$\underline{P_s}$	Power of sub-6G pilot signals (dBm)	10
$\sigma_n^2, \underline{\sigma_n^2}$	Noise power of mmWave, sub-6G system (dBm)	$-173.8 + 90 + 10 \log_{10}(W)$ $-173.8 + 90 + 10 \log_{10}(\underline{W})$
S, β	Number of candidate distances and correlation parameter of \mathcal{W}	7, 1.6

B. Performance Metrics and Baselines

To comprehensively assess the performance of proposed SCAN-BEST, we evaluate the following performance metrics:

- **Achieved coverage rate**, i.e., the complement of the probability (16), quantifying the probability that a beam in $\mathcal{C}_{\hat{\lambda}}(\hat{\mathbf{H}})$ satisfies the condition in (14) over the test dataset;
- **Achieved ϵ -suboptimal rate**, i.e., the complement of the probability (15), quantifying the probability that final selected beam \mathbf{f} is ϵ -suboptimal over the test dataset.

As for the predictor, we consider the following in the comparison:

- **Augmented discrete angle and delay transformation-based prediction (ADADT-P)**: ADADT-P begins by applying an augmented two-dimensional discrete Fourier transform [39] to the sub-6G channel estimates to extract angle and delay information as key features. These features are then fed into a neural network to predict the optimal near-field beam probabilities.
- **Sub-6G pilots-based beam prediction (SPBP)**: SPBP uses a neural network to directly predict the optimal near-field beam probabilities from received sub-6G pilot signals.

Both the detailed configurations and training settings of the above predictors are provided in Appendix C.

TABLE II
BASELINE METHODS

Method Category	Method	Predictor	candidate beam subset	MmWave Beam Training
In-band mmWave training baselines	EBS [9]	\times	\times	Exhaustive search with $N_t S$ pilots
	FNBS [9]	\times	\times	Two-stage search with $N_t + 3S$ pilots
Sub 6GHz-based baselines	SPBP + Top- K	SPBP	Top- K	Limited mmWave beam training within candidate beam subset
	SPBP + PS	SPBP	PS	
	ADADT-P + Top- K	ADADT-P	Top- K	
	ADADT-P + PS	ADADT-P	PS	
Our method	SCAN-BEST	SPBP ADADT-P	CRC (optimally weighted for covariate shifts)	

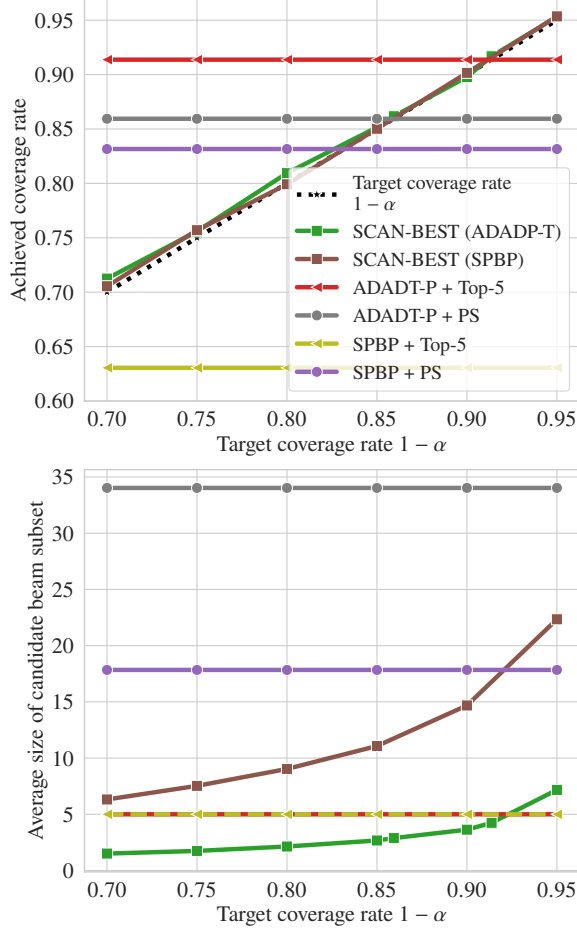


Fig. 6. Achieved coverage rates and average sizes of candidate beam subset of SCAN-BEST and baselines for $\epsilon = 0.15$.

As benchmarks, we consider two classical schemes to select the candidate beam subset based on the given predictor above:

- **Top- K selection [16]:** Identify the K beams with the highest predictive probabilities to form the candidate beam subset.
- **Probability sum (PS) selection [37]:** Choose the smallest set of beams whose cumulative predictive probability exceeds a predefined threshold (set to 0.99 unless otherwise specified) to form the candidate beam subset.

In Table. II, we summarize different combinations of predictor and candidate beam subset selection scheme. Furthermore,

we also consider two baseline methods that do not utilize sub-6G information: exhaustive beam search (EBS) and fast near-field beam search (FNBS), both proposed in [9].

C. Coverage Rate Guarantee of SCAN-BEST

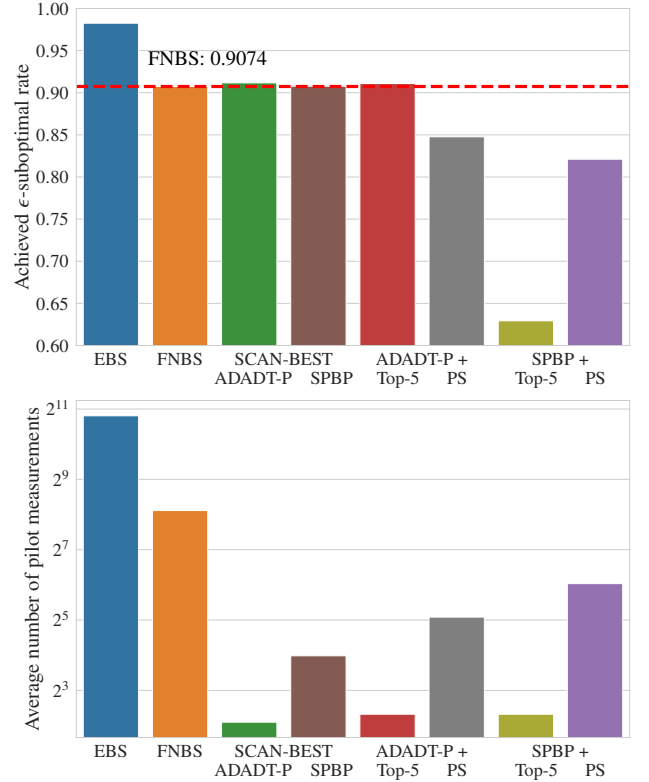


Fig. 7. Comparison of the average suboptimality ratio and of the number of pilot symbols for SCAN-BEST, mmWave-based, and sub 6GHz-based baselines.

To start, we evaluate the reliability guarantees provided by SCAN-BEST in term of coverage rate (16). Fig. 6 presents the achieved coverage rates, along with the sizes of the candidate beam subsets for SCAN-BEST and for sub 6GHz-based baselines when the suboptimality target is $\epsilon = 0.15$. For results with other values of ϵ , refer to Fig. 12 in Appendix C. Confirming theoretical properties of Proposition 1, with the help of CRC, both the predictors ADADT-P and SPBP can be calibrated to the target coverage rate by dynamically increasing

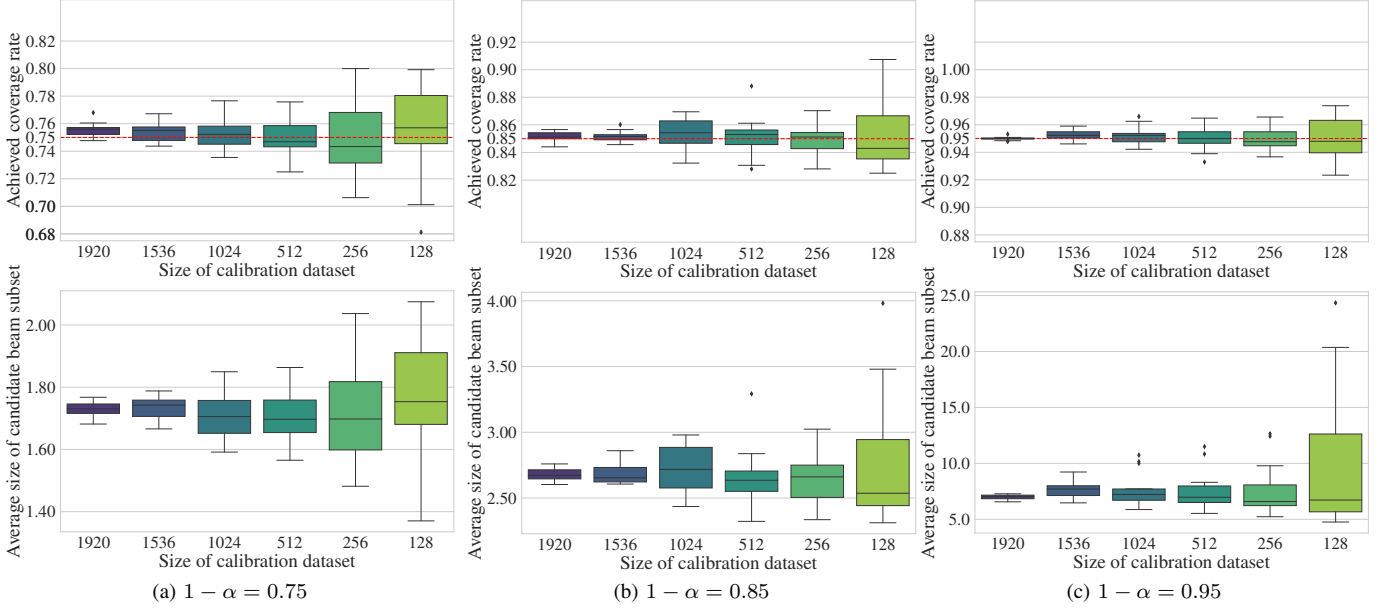


Fig. 8. Box plots for the achieved coverage rate and the size of the candidate beam subset under different calibration dataset sizes, with target coverage rates $1 - \alpha$ of (a) 0.75, (b) 0.85, and (c) 0.95. The red lines denote the target coverage rates $1 - \alpha$, while “M” indicates the mean.

the size of candidate beam subset. Thanks to the more use of a more effective predictor, SCAN-BEST (ADADT-P) requires a smaller candidate beam subset as compared to SCAN-BEST (SPBP) to achieve the same coverage rate.

In contrast, the baselines using candidate beam subsets constructed via Top- K or PS achieve only fixed coverage rates, as their candidate beam subsets cannot be dynamically adjusted to meet specific target coverage rates. Furthermore, when achieving the same coverage rate as ADADT-P + Top-5 and ADADT-P + PS, SCAN-BEST (ADADT-P) attains smaller candidate beam subsets. Specifically, the average sizes of the candidate beam subsets for ADADT-P + Top-5 and ADADT-P + PS=0.99 are 5 and 33.9 for $\alpha = 0.086$ and $\alpha = 0.106$, respectively, while those for SCAN-BEST (ADADT-P) are 4.2 and 2.8, respectively.

In addition, compared to in-band mmWave training baselines, SCAN-BEST achieves competitive performance with significantly fewer mmWave pilot symbols, as shown in Fig. 7. For example, FNBS achieves a ϵ -suboptimal rate of 0.9074 using 277 mmWave pilots, and then taking target coverage rate $1 - \alpha = 0.91$, SCAN-BEST (ADADT-P) and SCAN-BEST (SPBS) attain higher ϵ -suboptimal rates than FNBS, while requiring only an average of 4.2 and 15.8 mmWave pilots, respectively.

D. Impact of the Size of Calibration Dataset

Here, we analyze the achieved coverage rate and candidate beam subset size when varying the calibration dataset sizes. Fixing the suboptimality parameter $\epsilon = 0.15$ and the target coverage rates $1 - \alpha = 0.75, 0.85, 0.95$, and taking SCAN-BEST (ADADT-P) as an example, Fig. 8 presents key statistical characteristics of the achieved coverage rate and candidate beam subset size for different calibration dataset sizes. The box plots, showing median (horizontal line), first inter-quartile

intervals (box), and support (whiskers) are evaluated with 15 independent experiments. The results show that, regardless of the dataset size, the average achieved coverage rate remains above the target coverage rate. Larger dataset sizes offer more reliable guarantees for the coverage rate and a more stable size of the candidate beam subset. Finally, higher target coverage rates generally demand smaller calibration datasets. For instance, for the same calibration dataset size N_{cal} , the inter-quartile ranges of achieved coverage rates at $1 - \alpha = 0.95$ are narrower than those at $1 - \alpha = 0.75$ and $1 - \alpha = 0.85$.

E. Impact of Sub-6G System Parameters

1) *Impact of Sub-6G Channel Estimation Power:* Following the previous setting of $1 - \alpha = 0.91$ and $\epsilon = 0.15$, we investigate the impact of the sub-6G channel estimation power, P_s , on the performance of SCAN-BEST. Fig. 9 shows that both SCAN-BEST (ADADT-P) and SCAN-BEST (SPBP) reliably maintain coverage rate guarantee $1 - \alpha = 0.91$, regardless of the power P_s . When P_s decreases, the candidate beam subset dynamically expands to satisfy the target coverage rate. Furthermore, we assess the generalization capability of SCAN-BEST by applying ADADT-P trained at $P_s = 0$ dBm, denoted by “SCAN-BEST (ADADT-P-0dBm)”, to test on datasets characterized by different power P_s . It exhibits similar performance to SCAN-BEST, which is attributed to the fact that CRC is a model-free calibration approach. In contrast, baselines using the Top- K and PS candidate beam subsets inevitably experience performance degradation or fluctuation as the power P_s varies.

2) *Impact of the Number of Sub-6G Antennas:* Similarly, under the setting of $1 - \alpha = 0.91$ and $\epsilon = 0.15$, SCAN-BEST (ADADT-P) and SCAN-BEST (SPBP) provide a reliable coverage rate guarantee of 0.91, regardless of the number of antennas N_t , as shown in Fig. 10. In scenarios with low

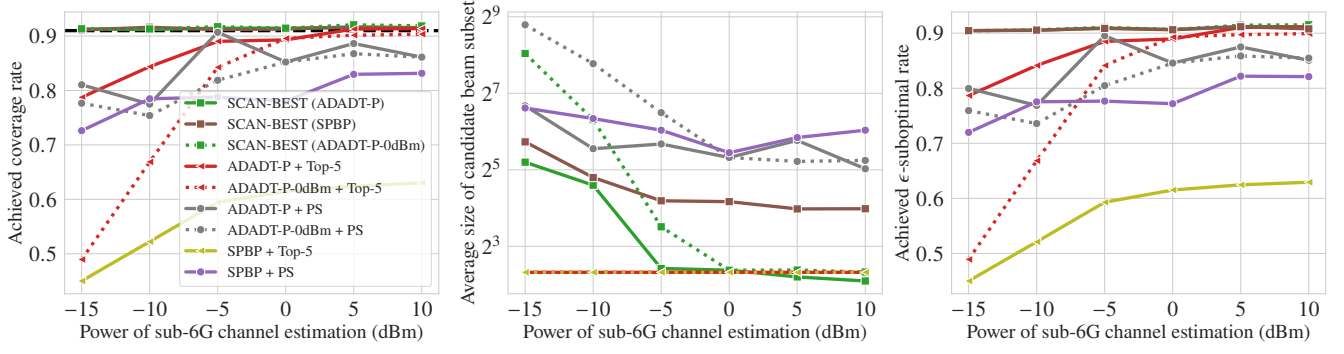


Fig. 9. Achieved coverage rates, average sizes of candidate beam subset, and average suboptimality ratios for SCAN-BEST and baselines under different numbers of sub-6G antennas.

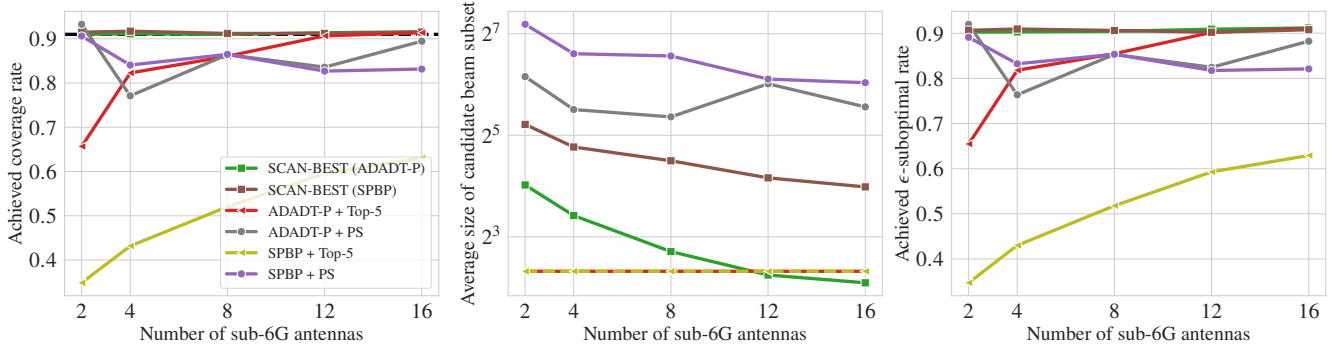


Fig. 10. Achieved coverage rates, average sizes of candidate beam subset, and average suboptimality ratios for SCAN-BEST and baselines under different powers of sub-6G channel estimation.

number of antennas N_t , which leads to poor angle resolution, both SCAN-BEST (ADADT-P) and SCAN-BEST (SPBP) dynamically expand their candidate beam subsets. However, SCAN-BEST (ADADT-P) maintains smaller candidate beam subsets due to the efficiency of the pre-processed ADADT.

F. Impact of Statistical Shifts between Calibration and test Datasets

In this subsection, we simulate a scenario in which the calibration and test data differ in the probability of LoS connectivity to validate the advantages of weighted CRC as compared to conventional CRC. Fixing the suboptimality parameter $\epsilon = 0.15$ and the target coverage rate $1 - \alpha = 0.85$, and taking ADADT-P as the predictor, Fig. 11 presents the achieved coverage rate and the size of the candidate beam subset for CRC and weighted CRC as a function of the LoS/NLoS ratio in the test distribution, when the LoS/NLoS ratio in the calibration distribution is fixed at 1. For a LoS probability p^{LoS} , the LoS/NLoS ratio is defined as $p^{\text{LoS}}/(1 - p^{\text{LoS}})$. All box plots are evaluated over 15 independent experiments.

As in [33], the probabilistic classifier $g(\cdot)$ is trained by minimizing the cross-entropy loss between the predicted probabilities and the corresponding binary labels, where a label of 1 indicates that the sample originates from the test distribution, and a label of 0 indicates that it is from the calibration distribution. The detailed configurations and training settings are provided in Appendix C. The results demonstrate that,

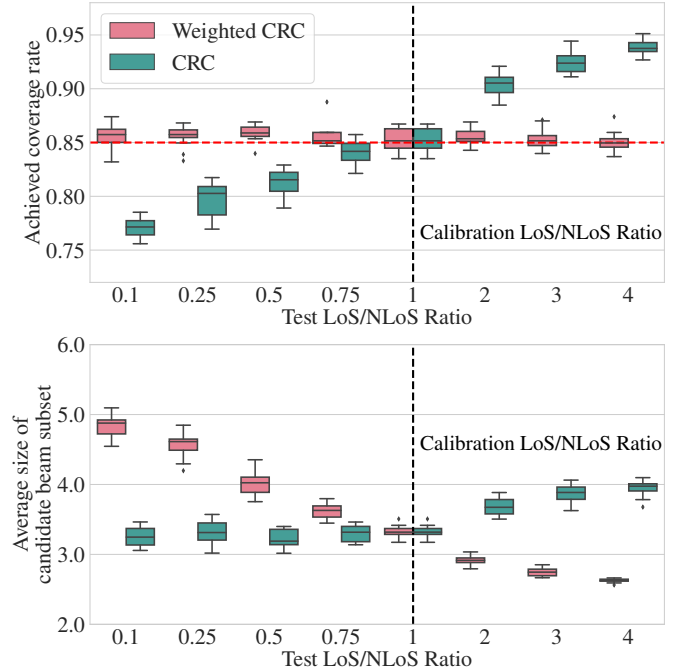


Fig. 11. Box plots of the achieved coverage rate and the size of the candidate beam subset under different LoS/NLoS ratios in the test data, with the LoS/NLoS ratio in the calibration data fixed at 1 (black line). The red lines denote the target coverage rates $1 - \alpha$.

regardless of the degree of misalignment between the calibration and test data, the weighted CRC method can effectively adapt to the test distribution, consistently achieving an average coverage rate higher than the target. In particular, when the proportion of LoS samples is large, weighted CRC provides reliable coverage guarantees and achieves a more stable candidate beam subset size than for lower probability, as the mapping from sub-6G information to mmWave beams becomes less uncertain. In contrast, CRC struggles to provide effective coverage in the covariate shift cases. Specifically, when the LoS/NLoS ratio is low, CRC fails to meet the coverage requirement. Conversely, when the LoS/NLoS ratio is high, it tends to produce an overly large candidate beam subset, which is inefficient for achieving the target coverage rate.

V. CONCLUSION

In this paper, we have proposed SCAN-BEST, a novel theoretically principled framework to enhance near-field beam selection while ensuring a guaranteed coverage rate. It wraps around any deep learning best-beam predictor, capturing the spatial-temporal correlation between sub-6G and mmWave channels and predicting of beam probabilities from sub-6G data. A CRC-based module, optionally weighted to cope with covariate shift, constructs a candidate beam subset with formal guarantees, which is then refined via limited mmWave beam training. Extensive simulations show that SCAN-BEST ensures statistical suboptimality requirements and is robust to various sub-6G configurations. Future work may explore CRC-based beamforming with multi-modal sensing in high-mobility settings.

APPENDIX A PROOF OF PROPOSITION 1

Given the pretrained distribution $\mathcal{P}_{\theta^*}(\hat{\mathbf{H}})$ and the definition of the candidate beam subset $\mathcal{C}_{\lambda}(\hat{\mathbf{H}})$ in (20). The miscoverage probability requirement in (16) can be expressed as

$$\Pr(\nexists \mathbf{w} \in \mathcal{C}_{\lambda}(\hat{\mathbf{H}}) : r(\mathbf{w}, \mathbf{H}) \geq 1 - \epsilon) \leq \alpha, \quad (30)$$

where the probability is taken over the underlying distribution of $\{\hat{\mathbf{H}}, \mathbf{H}\}$.

We define a loss function $\ell(\hat{\mathbf{H}}, \mathbf{H}, \lambda) \in \{0, 1\}$ as

$$\ell(\hat{\mathbf{H}}, \mathbf{H}, \lambda) = \mathbb{1}(\nexists \mathbf{w} \in \mathcal{C}_{\lambda}(\hat{\mathbf{H}}) : r(\mathbf{w}, \mathbf{H}) \geq 1 - \epsilon). \quad (31)$$

As a result, the miscoverage probability requirement in (16) is equivalent to

$$\Pr(\ell(\hat{\mathbf{H}}, \mathbf{H}, \lambda) = 1) \leq \alpha, \quad (32)$$

which can be expressed as

$$\mathbb{E}[\ell(\hat{\mathbf{H}}, \mathbf{H}, \lambda)] \leq \alpha. \quad (33)$$

Thus, the miscoverage probability requirement in (16) is equivalent to the risk control problem in (33).

The empirical risk function $\hat{R}(\lambda)$ in (21) can be written as

$$\hat{R}(\lambda) = \frac{1}{N_{\text{cal}}} \sum_{i=1}^{N_{\text{cal}}} \ell(\hat{\mathbf{H}}_i, \mathbf{H}_i, \lambda). \quad (34)$$

With a little abuse of notation, we denote $\ell(\hat{\mathbf{H}}_i, \mathbf{H}_i, \lambda)$ as $\ell_i(\lambda)$, hence $\hat{R}(\lambda)$ can be expressed as $\hat{R}(\lambda) = \sum_{i=1}^{N_{\text{cal}}} \ell_i(\lambda) / N_{\text{cal}}$. Here, we introduce an auxiliary risk function $\hat{R}_f(\lambda)$ accounting for both calibration samples $\{\hat{\mathbf{H}}_i, \mathbf{H}_i\}_{i=1}^{N_{\text{cal}}}$ and a future sample $\{\hat{\mathbf{H}}_{N_{\text{cal}}+1}, \mathbf{H}_{N_{\text{cal}}+1}\}$, which is given by

$$\hat{R}_f(\lambda) = \frac{1}{N_{\text{cal}} + 1} \sum_{i=1}^{N_{\text{cal}}+1} \ell_i(\lambda). \quad (35)$$

Proposition 3. *The functions $\ell_i(\lambda)$ is monotonically non-increasing w.r.t. λ .*

Proof. For an arbitrary pair $\{\hat{\mathbf{H}}_i, \mathbf{H}_i\}$, assume $\lambda_1 < \lambda_2$, and consider two candidate beam subsets $\mathcal{C}_{\lambda_1}(|\mathbf{G}_i|) = \{\mathbf{w}_{n,s} \in \mathcal{W} : u(n, s, \hat{\mathbf{H}}_i) \leq \lambda_1\}$ and $\mathcal{C}_{\lambda_2}(|\mathbf{G}_i|) = \{\mathbf{w}_{n,s} \in \mathcal{W} : u(n, s, \hat{\mathbf{H}}_i) \leq \lambda_2\}$. For any $\mathbf{w}_{n,s} \in \mathcal{C}_{\lambda_1}(\hat{\mathbf{H}}_i)$, it follows $u(n, s, \hat{\mathbf{H}}_i) \leq \lambda_1 \leq \lambda_2$, which implies $\mathbf{w}_{n,s} \in \mathcal{C}_{\lambda_2}(\hat{\mathbf{H}}_i)$. Hence, we have the implication

$$\lambda_1 < \lambda_2 \implies \mathcal{C}_{\lambda_1}(\hat{\mathbf{H}}_i) \subset \mathcal{C}_{\lambda_2}(\hat{\mathbf{H}}_i).$$

It can be also seen that the inequality $\ell_i(\lambda_1) \geq \ell_i(\lambda_2)$ holds. \square

We also have

$$\begin{aligned} \hat{R}_f(\lambda) &= \frac{N_{\text{cal}}}{N_{\text{cal}} + 1} \hat{R}(\lambda) + \frac{\ell_{N_{\text{cal}}+1}(\lambda)}{N_{\text{cal}} + 1} \\ &\stackrel{(a)}{\leq} \frac{N_{\text{cal}}}{N_{\text{cal}} + 1} \hat{R}(\lambda) + \frac{1}{N_{\text{cal}} + 1}, \end{aligned} \quad (36)$$

where condition (a) holds because $\ell_{N_{\text{cal}}+1}(\lambda) \in \{0, 1\} \leq 1$. Then, using the optimized $\hat{\lambda}$ in (22), we obtain that

$$\frac{N_{\text{cal}}}{N_{\text{cal}} + 1} \hat{R}(\hat{\lambda}) + \frac{1}{N_{\text{cal}} + 1} \leq \alpha. \quad (37)$$

According to the inequality in (36), this implies that

$$\begin{aligned} \hat{R}_f(\hat{\lambda}) &\leq \frac{N_{\text{cal}}}{N_{\text{cal}} + 1} \hat{R}(\hat{\lambda}) + \frac{1}{N_{\text{cal}} + 1} \leq \alpha \implies \\ \hat{R}_f(\hat{\lambda}) &\leq \alpha. \end{aligned} \quad (38)$$

Introducing $\hat{\lambda}^\downarrow = \inf\{\lambda \in \mathbb{R} : \hat{R}_f(\lambda) \leq \alpha\}$, we know that $\hat{\lambda}^\downarrow \leq \hat{\lambda}$. Thus, according to Proposition 3, we obtain

$$\mathbb{E}[\ell_{N_{\text{cal}}+1}(\hat{\lambda})] \leq \mathbb{E}[\ell_{N_{\text{cal}}+1}(\hat{\lambda}^\downarrow)]. \quad (39)$$

In mathematics, a bag (also called a multiset) is a collection where elements can appear more than once.

Lemma 1 (From [33]). *If the random variables x_1, \dots, x_n, x_{n+1} are exchangeable, and conditioned on the bag of realization of $\{x_1, \dots, x_n, x_{n+1}\}$, the random variable x_{n+1} is uniformly distributed in the set $\{x_1, \dots, x_n, x_{n+1}\}$.*

Since the calibration samples $\{\hat{\mathbf{H}}_i, \mathbf{H}_i\}_{i=1}^{N_{\text{cal}}}$ and the future sample $\{\hat{\mathbf{H}}_{N_{\text{cal}}+1}, \mathbf{H}_{N_{\text{cal}}+1}\}$ are i.i.d. from the same scenario, they are exchangeable. According to the exchangeability-preserving theorem (Theorem 3 in [20]), the functions $\ell_1(\lambda), \dots, \ell_{N_{\text{cal}}}(\lambda), \ell_{N_{\text{cal}}+1}(\lambda)$ are also exchangeable, and we obtain

$$\ell_{N_{\text{cal}}+1}(\lambda) \sim \text{Uniform}(\ell_1(\lambda), \dots, \ell_{N_{\text{cal}}}(\lambda), \ell_{N_{\text{cal}}+1}(\lambda)). \quad (40)$$

Conditioned on the bag of realization of $\{\ell_1(\lambda), \dots, \ell_{N_{\text{cal}}}(\lambda),$

$\ell_{N_{\text{cal}}+1}(\lambda)\}$, when $\lambda = \hat{\lambda}'$, we have

$$\mathbb{E} \left[\ell_{N_{\text{cal}}+1}(\hat{\lambda}^\downarrow) \right] = \frac{1}{N_{\text{cal}}+1} \sum_{i=1}^{N_{\text{cal}}+1} \ell_i(\hat{\lambda}^\downarrow) = \hat{R}_f(\hat{\lambda}^\downarrow) \stackrel{(b)}{\leq} \alpha \implies \mathbb{E}[\ell_{N_{\text{cal}}+1}(\hat{\lambda}^\downarrow)] \leq \alpha, \quad (41)$$

where the condition (b) holds according to the definition of $\hat{\lambda}^\downarrow$. Finally, according to (39), we obtain the following result:

$$\mathbb{E}[\ell_{N_{\text{cal}}+1}(\hat{\lambda})] \leq \alpha. \quad (42)$$

APPENDIX B

PROOF OF PROPOSITION 2

For the samples in the calibration dataset, we denote their loss as $\ell_i(\lambda)$ for $i = 1, \dots, N_{\text{cal}}$, while, for the future test sample $\{\hat{\mathbf{H}}, \mathbf{H}'\}$, we denote its loss as $\ell'(\lambda)$. We have $\tilde{R}(\lambda) = \sum_{i=1}^{N_{\text{cal}}} \omega_i \ell_i(\lambda)$. Define an auxiliary risk function $\tilde{R}_f(\lambda)$ accounting for both calibration samples $\{\hat{\mathbf{H}}, \mathbf{H}'\}_{i=1}^{N_{\text{cal}}}$ and the future test sample $\{\hat{\mathbf{H}}, \mathbf{H}'\}$ as

$$\tilde{R}_f(\lambda) = \sum_{i=1}^{N_{\text{cal}}} \omega_i \ell_i(\lambda) + \omega' \ell'(\lambda). \quad (43)$$

Accordingly, we obtain the inequality

$$\tilde{R}_f(\lambda) \stackrel{(a)}{\leq} \tilde{R}(\lambda) + \omega', \quad (44)$$

where condition (a) holds because $\ell'(\lambda) \in \{0, 1\} \leq 1$. When using the optimized $\hat{\lambda}$ in (26), we have

$$\tilde{R}(\hat{\lambda}) + \omega' \leq \alpha. \quad (45)$$

According to the inequality in (44), this indicates that

$$\tilde{R}_f(\lambda) \leq \alpha. \quad (46)$$

Introducing $\hat{\lambda}^\downarrow = \inf\{\lambda \in \mathbb{R} : \tilde{R}_f \leq \alpha\}$, it implies $\hat{\lambda}^\downarrow \leq \hat{\lambda}$. Then, according to Proposition (3), we conclude

$$\mathbb{E}[\ell'(\hat{\lambda})] \leq \mathbb{E}[\ell'(\hat{\lambda}^\downarrow)]. \quad (47)$$

Lemma 2 (Lemma 3 of [33]). *Let $z = (x, y)$. Suppose the random variables z_1, \dots, z_n are from the calibration distribution $\Gamma_c(z)$, and z' is from the test distribution $\Gamma_t(z)$. z_1, \dots, z_n, z' are conditioned on the bag of realization of $\{z_1, \dots, z_n, z'\}$. Define the weights*

$$\omega_i = \frac{p_i}{\sum_{j=1}^n p_j + p'}, \quad \omega' = \frac{p'}{\sum_{j=1}^n p_j + p'}, \quad (48)$$

where

$$p_i = \frac{\Gamma_t(z_i)}{\Gamma_c(z_i)}, \quad p' = \frac{\Gamma_t(z')}{\Gamma_c(z')}, \quad (49)$$

for $i = 1, \dots, n$. Then, the test sample z' is distributed as

$$z' \sim \sum_{i=1}^n \omega_i \delta_{z_i} + \omega' \delta_{z'}, \quad (50)$$

where δ_z denotes the Dirac measure at z . Moreover, for any non-random loss function $\ell(\cdot)$ over z , it follows that

$$\ell(z') \sim \sum_{i=1}^n \omega_i \delta_{\ell(z_i)} + \omega' \delta_{\ell(z')}. \quad (51)$$

In the considered scenario, the conditional distribution of \mathbf{H} given $\hat{\mathbf{H}}$ is assumed to remain the same in the calibration and test datasets [16]. Under this covariate shift assumption, the weights ω_1, \dots, ω' can be computed as in (23). Based on

TABLE III
ADADT-P PARAMETERS

Input/Output Channel	Layers	Convolution Kernels
(1, 32)	{Conv2D, BatchNorm2D, ReLU} \times 2, MaxPool2D	(8, 4)
(32, 64)	idem	(5, 3)
(64, 128)	idem	(5, 3)
(128, 256)	idem	(5, 3)
(256, 256)	Conv2D, BatchNorm2D	(3, 3)
(256, 128)	Upsample, Conv2D, BatchNorm2D, ReLU Conv2D, BatchNorm2D	(3, 3)
(128, 64)	idem	(7, 3)
(64, 32)	idem	(7, 3)
(32, 16)	idem	(7, 3)
(16, 8)	idem	(7, 3)
(8, 1)	Conv2D	(7, 3)
/	Flatten, Softmax, Reshape	/

the loss function $\ell_\lambda(\cdot)$ defined in (31), and setting $\lambda = \hat{\lambda}^\downarrow$, we have

$$\ell'(\hat{\lambda}^\downarrow) \sim \sum_{i=1}^n \omega_i \delta_{\ell_i(\hat{\lambda}^\downarrow)} + \omega' \delta_{\ell'(\hat{\lambda}^\downarrow)} \implies$$

$$\mathbb{E}[\ell'(\hat{\lambda}^\downarrow)] = \sum_{i=1}^n \omega_i \ell_i(\hat{\lambda}^\downarrow) + \omega' \ell'(\hat{\lambda}^\downarrow) = \tilde{R}_f(\hat{\lambda}^\downarrow) \stackrel{(b)}{\leq} \alpha \implies \mathbb{E}[\ell'(\hat{\lambda}^\downarrow)] \leq \alpha, \quad (52)$$

where condition (b) follows from the definition of $\hat{\lambda}^\downarrow$. Finally, by the inequality in (47), we conclude:

$$\mathbb{E}[\ell'(\hat{\lambda})] \leq \alpha. \quad (53)$$

APPENDIX C

ADDITIONAL EXPERIMENTAL MATERIALS

To balance performance and complexity, both the predictors ADADT-P and SPBP are implemented as 2D CNN architectures, whose parameters are provided in Tables III and IV, respectively. Both of them are trained using the Adam optimizer with a batch size of 128, an initial learning rate of 0.0002, and the learning rate scheduler ‘‘ReduceLROnPlateau’’ [40]. This scheduler automatically reduces the learning rate when the model’s performance on the validation set ceases to improve or demonstrates only marginal improvements over a specified number of training epochs. Both the maximum training epochs of ADADT-P and SPBP are set to 200, and, to prevent overfitting, a classical early stopping criterion is adopted, which stops the training process if the validation loss does not improve for a certain number of epochs. The probabilistic classifier $g(\cdot)$ used in the weighted CRC, is also implemented as a 2D CNN architecture with its configuration in Table V. The optimizer, batch size, and learning rate schedule, are the same as for the predictors, and the initial learning rate is set as 0.0004.

Moreover, in Fig. 12, we present the additional results varying the suboptimality parameter ϵ value.

REFERENCES

- [1] C. Liu, M. Li, S. V. Hanly, P. Whiting, and I. B. Collings, ‘‘Millimeter-wave small cells: Base station discovery, beam alignment, and system design challenges,’’ *IEEE Wireless Commun.*, vol. 25, no. 4, pp. 40–46, 2018.

TABLE IV
SPBP PARAMETERS

Input/Output Channel	Layers	Convolution Kernels
(1, 32)	{Conv2D, BatchNorm2D, ReLU} \times 2, MaxPool2D	(2, 4)
(32, 64)	idem	(2, 4)
(64, 128)	idem	(2, 4)
(128, 128)	idem	(2, 4)
(128, 64)	Upsample, Conv2D, BatchNorm2D, ReLU	(3, 3)
(64, 32)	Conv2D, BatchNorm2D	(7, 3)
(32, 16)	idem	(7, 3)
(16, 8)	idem	(7, 3)
(8, 1)	Conv2D	(7, 3)
/	Flatten, Softmax, Reshape	/

TABLE V
PROBABILISTIC CLASSIFIER PARAMETERS

Input/Output Channel	Layers	Convolution Kernels
(1, 32)	Conv2D, BatchNorm2D, ReLU, MaxPool2D	(3, 3)
(32, 64)	idem	(3, 3)
(64, 128)	idem	(3, 3)
(128, 256)	Conv2D, BatchNorm2D, ReLU, AdaptiveAvgPool2D	(3, 3)
(256, 64)	Flatten, Linear, ReLU	/
(64, 1)	Linear, Sigmoid	/

- [2] Y. Liu, C. Ouyang, Z. Ding, and R. Schober, "The road to next-generation multiple access: A 50-year tutorial review," *Proc. IEEE*, vol. 112, no. 9, pp. 1100–1148, 2024.
- [3] M. Cui, Z. Wu, Y. Lu, X. Wei, and L. Dai, "Near-field mimo communications for 6G: Fundamentals, challenges, potentials, and future directions," *IEEE Commun. Mag.*, vol. 61, no. 1, pp. 40–46, 2022.
- [4] Y. Liu, W. Deng, M. Li, and M.-J. Zhao, "Position-aware beam training for near-field millimeter-wave xl-mimo communications," in *Veh. Technol. Conf.*, 2024, pp. 1–6.
- [5] Y. Liu, C. Ouyang, Z. Wang, J. Xu, X. Mu, and A. L. Swindlehurst, "Near-field communications: A comprehensive survey," *arXiv preprint arXiv:2401.05900*, 2024.
- [6] M. K. Samimi and T. S. Rappaport, "3-D millimeter-wave statistical channel model for 5G wireless system design," *IEEE Trans. Microwave Theory Tech.*, vol. 64, no. 7, pp. 2207–2225, 2016.
- [7] K. Vuckovic, M. B. Mashhadi, F. Hejazi, N. Rahnavard, and A. Alkhateeb, "Paramount: Towards generalizable deep learning for mmwave beam selection using sub-6GHz channel measurements," *IEEE Trans. Wireless Commun.*, pp. 1–1, 2023.
- [8] M. Cui and L. Dai, "Channel Estimation for Extremely Large-Scale MIMO: Far-Field or Near-Field?" *IEEE Trans. Commun.*, vol. 70, no. 4, pp. 2663–2677, Apr. 2022.
- [9] Y. Zhang, X. Wu, and C. You, "Fast Near-Field Beam Training for Extremely Large-Scale Array," *IEEE Wireless Commun. Lett.*, vol. 11, no. 12, pp. 2625–2629, Dec. 2022.
- [10] C. Wu, C. You, Y. Liu, L. Chen, and S. Shi, "Two-stage hierarchical beam training for near-field communications," *IEEE Trans. Veh. Technol.*, vol. 73, no. 2, pp. 2032–2044, 2024.
- [11] G. Jiang and C. Qi, "Near-field beam training based on deep learning for extremely large-scale mimo," *IEEE Commun. Lett.*, vol. 27, no. 8, pp. 2063–2067, 2023.
- [12] W. Liu, H. Ren, C. Pan, and J. Wang, "Deep learning based beam training for extremely large-scale massive mimo in near-field domain," *IEEE Commun. Lett.*, vol. 27, no. 1, pp. 170–174, 2023.
- [13] G. Zhang, Q. Hu, Z. Qin, Y. Cai, G. Yu, and X. Tao, "A unified multi-task semantic communication system for multimodal data," *IEEE Trans. Commun.*, vol. 72, no. 7, pp. 4101–4116, 2024.
- [14] Remcom, "Wireless InSite," <http://www.remcom.com/wireless-insite>.
- [15] A. Ali, N. González-Prelcic, and R. W. Heath, "Millimeter wave beam-selection using out-of-band spatial information," *IEEE Trans. Wireless Commun.*, vol. 17, no. 2, pp. 1038–1052, 2017.
- [16] M. Alrabeiah and A. Alkhateeb, "Deep learning for mmwave beam and blockage prediction using sub-6 GHz channels," *IEEE Trans. Commun.*, vol. 68, no. 9, pp. 5504–5518, 2020.
- [17] W. Deng, M. Li, Y. Liu, M.-M. Zhao, and M. Lei, "Enhancing mmwave beam prediction through deep learning with sub-6 GHz channel estimate," in *IEEE Wireless Commun. Networking Conf.*, 2024, pp. 1–6.
- [18] W. Deng, M. Li, M.-M. Zhao, M.-J. Zhao, and O. Simeone, "CSI transfer from sub-6G to mmwave: Reduced-overhead multi-user hybrid beamforming," *IEEE J. Sel. Areas Commun.*, vol. 43, no. 3, pp. 973–987, 2025.
- [19] H. Wu, L. Lu, and Z. Wang, "Near-field channel estimation in dual-band xl-mimo with side information-assisted compressed sensing," *IEEE Trans. Commun.*, pp. 1–1, 2024.
- [20] A. K. Kuchibhotla, "Exchangeability, conformal prediction, and rank tests," *arXiv preprint arXiv:2005.06095*, 2020.
- [21] A. N. Angelopoulos, S. Bates, A. Fisch, L. Lei, and T. Schuster, "Conformal risk control," *arXiv preprint arXiv:2208.02814*, 2022.
- [22] Y. Xu, M. Ying, W. Guo, and Z. Wei, "Two-stage risk control with application to ranked retrieval," *arXiv preprint arXiv:2404.17769*, 2024.
- [23] R. Hulsman, V. Comte, L. Bertolini, T. Wiesenthal, A. P. Gallardo, and M. Ceresa, "Conformal risk control for pulmonary nodule detection," *arXiv preprint arXiv:2412.20167*, 2024.
- [24] S. Bai, X. Zheng, and D. D. Zeng, "Crc-sgad: Conformal risk control for supervised graph anomaly detection," *arXiv preprint arXiv:2504.02248*, 2025.
- [25] M. Zecchin, S. Park, and O. Simeone, "Forking uncertainties: Reliable prediction and model predictive control with sequence models via conformal risk control," *IEEE J. Sel. Areas Inf. Theory*, vol. 5, pp. 44–61, 2024.
- [26] M. Zhu, M. Zecchin, S. Park, C. Guo, C. Feng, P. Popovski, and O. Simeone, "Conformal distributed remote inference in sensor networks under reliability and communication constraints," *arXiv preprint arXiv:2409.07902*, 2024.
- [27] K. M. Cohen, S. Park, O. Simeone, and S. S. Shitz, "Cross-validation conformal risk control," in *IEEE Int. Symp. Inf. Theory*. IEEE, 2024, pp. 250–255.
- [28] A. Angelopoulos, E. Candes, and R. J. Tibshirani, "Conformal pid control for time series prediction," *Adv. neural inf. proces. syst.*, vol. 36, pp. 23 047–23 074, 2023.
- [29] M. Zecchin and O. Simeone, "Localized adaptive risk control," *arXiv preprint arXiv:2405.07976*, 2024.
- [30] K. M. Cohen, S. Park, O. Simeone, and S. Shamai Shitz, "Calibrating ai models for wireless communications via conformal prediction," *IEEE trans. mach. learn. commun. netw.*, vol. 1, pp. 296–312, 2023.
- [31] M. Zhu, M. Zecchin, S. Park, C. Guo, C. Feng, and O. Simeone, "Federated inference with reliable uncertainty quantification over wireless channels via conformal prediction," *IEEE Trans. Signal Processing*, vol. 72, pp. 1235–1250, 2024.
- [32] H. Wen, H. Xing, and O. Simeone, "Distributed conformal prediction via message passing," *arXiv preprint arXiv:2501.14544*, 2025.
- [33] R. J. Tibshirani, R. Foygel Barber, E. Candes, and A. Ramdas, "Conformal prediction under covariate shift," *Adv. neural inf. proces. syst.*, vol. 32, 2019.
- [34] B. Wang, H. Li, S. Shen, Z. Cheng, and B. Clerckx, "A dual-function radar-communication system empowered by beyond diagonal reconfigurable intelligent surface," *IEEE Trans. Commun.*, pp. 1–1, 2024.
- [35] X. Peng, L. Zhao, Y. Jiang, J. Liu, and W. Li, "Channel Estimation for Extremely Large-Scale Massive MIMO Systems in Hybrid-Field Channel," in *IEEE/CIC Int. Conf. Commun. China*. Dalian, China: IEEE, Aug. 2023, pp. 1–6.
- [36] W. Liu, C. Pan, H. Ren, C.-X. Wang, J. Wang, and X. You, "Nmbsnet: Efficient near-field mmwave beam training for multiuser ofdm systems using sub-6 ghz pilots," *IEEE Trans. Commun.*, pp. 1–1, 2024.
- [37] K. Ma, S. Du, H. Zou, W. Tian, Z. Wang, and S. Chen, "Deep learning assisted mmwave beam prediction for heterogeneous networks: A dual-band fusion approach," *IEEE Trans. Commun.*, vol. 71, no. 1, pp. 115–130, 2022.
- [38] O. Simeone, "Classical and quantum uncertainty, information, and correlation," <https://sites.google.com/view/osvaldosimeone/cqit>, 2024, in preparation.
- [39] X. Sun, X. Gao, G. Y. Li, and W. Han, "Single-site localization based on a new type of fingerprint for massive mimo-ofdm systems," *IEEE Trans. Veh. Technol.*, vol. 67, no. 7, pp. 6134–6145, 2018.
- [40] "ReduceLROnPlateau — PyTorch 2.1 documentation," [Online]. Available: https://pytorch.org/docs/stable/generated/torch.optim.lr_scheduler.ReduceLROnPlateau.html

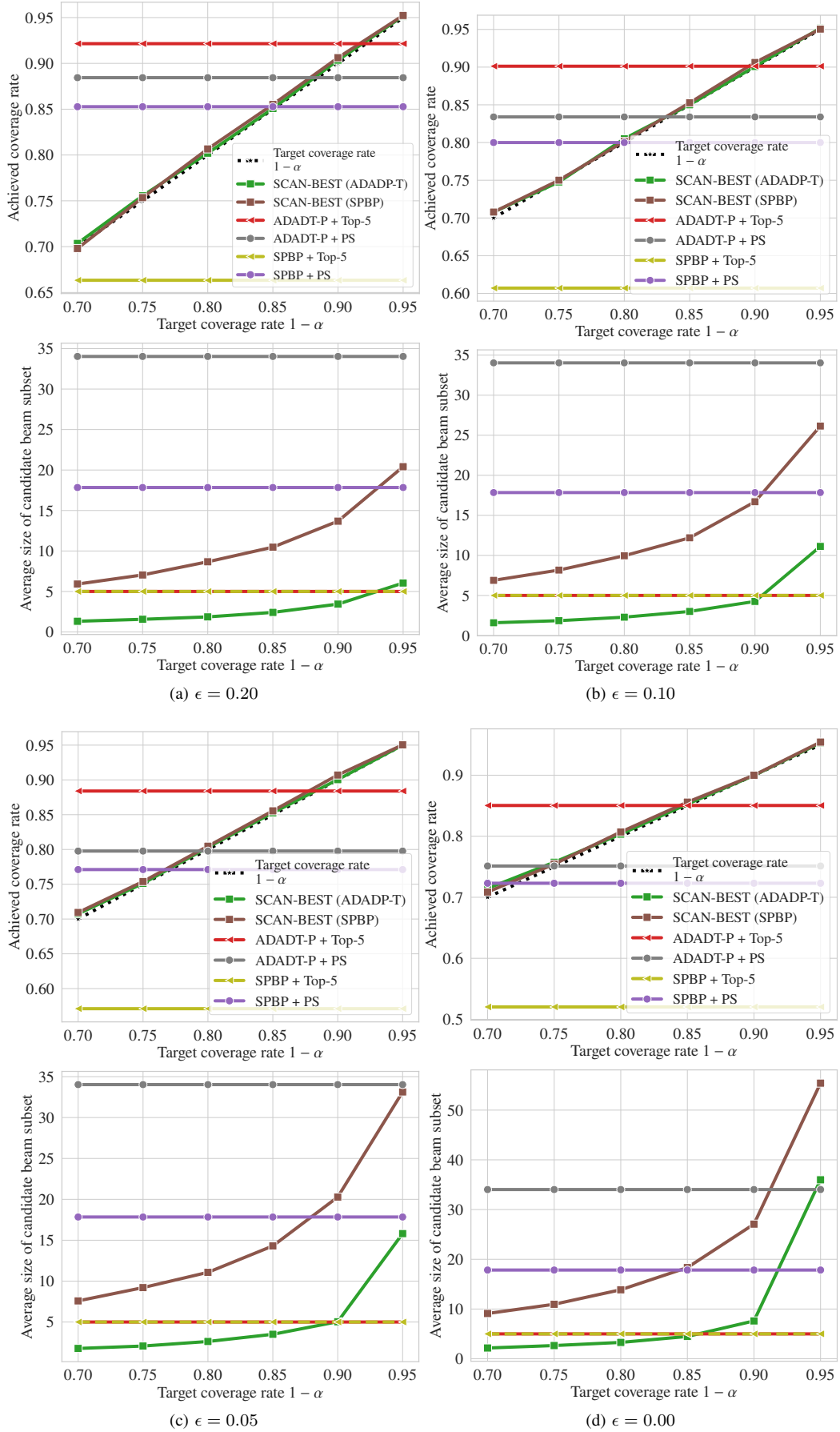


Fig. 12. Achieved coverage rates and average sizes of candidate beam subset of SCAN-BEST and baselines for $\epsilon = 0.20, 0.10, 0.05, 0.00$.